Electrostatic plasma turbulence in the topside equatorial *F* region ionosphere

D. L. Hysell and E. B. Shume

Department of Physics and Astronomy, Clemson University, Clemson, South Carolina

Short title: TURBULENCE IN THE F REGION IONOSPHERE

Abstract.

Two-dimensional, turbulent plasma flows in the topside equatorial *F* region ionosphere associated with fully-developed equatorial spread *F* are analyzed and simulated numerically. In the inertially dominated flow regime, the governing equations of motion resemble the Navier Stokes equation but are cubicly nonlinear. Large amplitude density irregularities are prerequisite for inertial effects to be important, but when these are present, the third-order nonlinear effects become significant, mean-squared velocity and vorticity cease to be conserved by nonlinear mode coupling, and the foundations of the turbulent cascade theory of *Kraichnan* [1967] are undermined. Nonetheless, one-dimensional, angle-averaged velocity spectra computed from simulated flows exhibit similarity ranges with $k^{-5/3}$ and k^{-3} power laws, resembling inertial ranges and suggesting turbulent cascades. Invariants of the flow (quantities conserved by nonlinear mode coupling) are found which are generalizations of the quadratic forms of kinetic energy and enstrophy and which are dimensionally equivalent to them. Statistical properties of the flow appear to permit turbulent cascades to arise.

1. Introduction

During equatorial spread *F* (ESF) conditions, plasma irregularities created by ionospheric interchange instabilities penetrate past the *F* region peak into the topside and into the inertial regime. This is the high-altitude flow regime where ion inertia is thought to compete with collisional effects, leading to a more complicated plasma flow than is observed at lower altitudes. It has been argued that the resulting flow should exhibit characteristics of classical, neutral, two-dimensional turbulence including turbulent cascades [*Kelley and Ott*, 1978; *Kintner and Seyler*, 1985; *Hassam et al.*, 1986; *Zargham and Seyler*, 1989; *McDaniel and Hysell*, 1997]. The bases for this argument are the similarity between the equations of motion governing the inertial regime plasma and the Navier Stokes equation along with what appear to be universal similarity ranges in the spectra of some topside plasma density fluctuation measurements. If turbulence arises in the inertial regime, the dynamics and kinematics of the plasma irregularities in question should be measurably affected. However, inertial regime irregularities have not been as thoroughly investigated as their collisional regime relatives, owing to the scarcity of data from instrumented spacecraft flying in the appropriate altitude range. The evidence for an actual turbulent cascade in the topside ionosphere during ESF is inconclusive and lacks a theoretical foundation. In this paper, we attempt to establish the foundation.

After *Woodman and La Hoz* [1976] presented compelling evidence that interchange instabilities drive ESF, several research groups developed numerical simulations of ionospheric interchange instabilities and reproduced many of the characteristics of spread *F*

seen at Jicamarca and elsewhere (see reviews by *Ossakow* [1981]). Most of this numerical work focused on instabilities in the collisional regime. *Hassam et al.* [1986] were the first to study inertial regime flows numerically. The flow they simulated was isotropic in the plane perpendicular to $\mathbf{B}$, in contrast to the anisotropic flows characteristic of the collisional regime, and the one-dimensional potential spectra they calculated obeyed Kolmogorov scaling, suggesting an energy cascade. Their numerical calculations did not include small scales where an enstrophy cascade range might have been found. *Zargham and Seyler* [1989] also studied the dynamics of collisional and inertial regime flows, this time over a wide range of spatial scale sizes. Their two-dimensional inertial regime simulations produced irregularities with one-dimensional energy (mean-squared velocity) spectra exhibiting pairs of inertial ranges. The slopes of these spectral ranges were $k^{-5/3}$ and k^{-3}, implying, respectively, the existence of energy and enstrophy cascades as predicted by *Kraichnan* [1967] and *Kraichnan and Montgomery* [1980]. *Matthaeus et al.* [1991] and *Montgomery et al.* [1992] investigated the long-term state of decaying two-dimensional Navier Stokes turbulence computationally. They found that vortex merging occurs until a single pair of large-scale counter rotating vortices remain. At that time, the enstrophy in the system has all dissipated, leaving no mechanism for the dissipation of the remaining energy, which has cascaded to large scales. *Hossain et al.* [1983] also examined the late-time behavior of simulations of the forced Navier Stokes equations and found that the asymptotic state is dominated by the fundamental mode. The inverse cascade of energy ultimately ceases as the outer scale approaches the finite simulation size, at which time the total energy stops growing and becomes dissipatively limited. However, all of these investigators neglected nonlinearities beyond second order in their model equations

which consequently assumed a form very similar to the Navier Stokes equation for neutral fluid turbulence. The applicability of their results to the topside ionosphere is limited to flows with small density perturbations. As discussed below, such flows would likely be collisionally dominated in nature.

Recently, *McDaniel and Hysell* [1997] investigated the role of ion inertia in topside ESF. They used the model for two-dimensional plasma turbulence described in section 2 of this paper but generalized it for application to a three-dimensional ionosphere with a flux tube integration procedure similar to the one introduced by *Haerendel* [1973]. Their analysis was dynamically self-consistent and so improved upon that of *Sultan* [1996]. They concluded that:

1. The effects of ion inertia can compete with collisional effects in plasma flows on magnetic flux tubes with apex heights between about 600 and 1000 km in the time interval beginning after sunset and lasting for an hour or more. The precise window of times and apex altitudes depends on the longitude, season, and phase of the solar cycle.

2. Large-amplitude ($\delta n/n \gtrsim$ 50%) irregularities in the plasma density are required for inertial effects to be important in nature since these give rise to strong convection and to polarization currents able to compete with Pedersen currents in determining the dynamics of the flow.

3. Although the model describing the turbulence is similar to the Navier Stokes equation in two dimensions, the presence of coupling between the plasma density, velocity, and vorticity in the model, together with the requirement that the density be strongly nonuniform, differentiate it from Navier Stokes. The analogy between Navier Stokes

and plasma turbulence is therefore imperfect, and it is not obvious that inertial range spectra should emerge in spacecraft measurements of topside spread *F* flows.

4. Nonetheless, plasma density data from the DE II satellite showed evidence of universal, inertial range spectra with $k^{-5/3}$ slopes for scale sizes larger than about 1 km in regions of strong plasma irregularities falling into the predicted apex altitude/local time window.

At about the same time, however, *Jahn and LaBelle* [1998] also sought evidence for an inertial flow regime in observations of topside spread *F* irregularities made with an instrumented sounding rocket flown from Brazil during project Guará. The plasma structures they observed where highly coherent and shock-like at all altitudes between about 300 and 1000 km. They were unable to differentiate qualitatively or quantitatively between plasma density and electric field data taken at low and high altitudes, and there was no unambiguous evidence of inertial range spectra to be found in their data. However, the amplitudes of the plasma irregularities encountered by their rocket near and above 600 km were relatively small ($\delta n/n < 50\%$), and the convection within the topside flow was quite weak [*Jahn and LaBelle*, 1997]. It is therefore possible that the flow they investigated was nowhere inertially dominated.

The literature on two-dimensional turbulent hydrodynamics is vast and falls into two main categories. The first and, by far, the larger of these addresses incompressible flows with nearly uniform densities in which density irregularities act as passive tracers of the flow. Navier Stokes turbulence belongs to this category. The second deals with compressible flows with potentially large density irregularities and focuses primarily on the problem of

acoustic turbulence. (See, for example, *Stanisic* [1988] and *Van Beeck and Benocci* [2000] for extensive reviews.) Relatively little is known about this problem. Inertial-regime flow in the ionosphere is characterized by the nearly incompressible convection of large amplitude density irregularities and therefore falls into neither of these categories. It is related to MHD turbulence but does not involve the complicating issues of magnetic energy density and cross-helicity (see review by *Zhou and Matthaeus* [1990]).

Here, we consider the problem of two-dimensional turbulence in weakly-collisional guiding center plasma flows with strong density irregularities. We begin by reviewing a simple model of the flow appropriate for the equatorial *F* region ionosphere. The model retains nonlinearities up to third order. Computer simulations of the model will be shown to produce density and energy (mean-squared velocity) spectra qualitatively similar to those associated with ordinary, two-dimensional Navier Stokes turbulence. We identify the invariants for the system in the unforced, nondissipative limit. An interpretation of the inertial ranges evident in the simulations results is provided which hinges on the statistical nature of the turbulence.

2. Fluid Model

Deriving model equations for the ionospheric plasma highlights the distinction between the collisional and inertial regimes and motivates the analysis to follow. The model considered is similar to those developed by [*Ott*, 1978], [*Kintner and Seyler*, 1985], and *Zargham and Seyler* [1989]. It is two dimensional in the plane perpendicular to $\mathbf{B}$. The electrostatic model is based on the fluid momentum equations for ions and nearly massless electrons. It assumes

slow spatial variations in the background collision frequencies and magnetic induction.

$$0 = -\nabla p_e - ne(\mathbf{E} + \mathbf{v}_e \times \mathbf{B}) - nm_e \nu_{en} \mathbf{v}_e \quad (1)$$

$$nm_i \left(\frac{\partial}{\partial t} + \mathbf{v}_i \cdot \nabla \right) \mathbf{v}_i = -\nabla p_i + ne(\mathbf{E} + \mathbf{v}_i \times \mathbf{B}) - nm_i \nu_{in} \mathbf{v}_i + nm_i \mathbf{g} + nm_i \eta \nabla^2 \mathbf{v}_i \quad (2)$$

Here, n is the plasma number density, $\mathbf{v}$ is the guiding-center velocity for electrons and ions, p is the pressure, and the other terms have their usual meaning. Ion-neutral and electron-neutral collisions are represented by ν_{in} and ν_{en}, respectively. The latter are retained only because they ultimately determine the molecular diffusivity in the plasma. Coulomb collisions are neglected except for the dependence of the kinematic viscosity η on ion-ion collisions. Charge neutrality implies that the current is solenoidal, which further implies that the $\mathbf{J} \times \mathbf{B}$ force is irrotational and allows us to write $\mathbf{J} \times \mathbf{B} = -B \nabla \xi$. Summing the electron and ion momentum equations then produces a single-fluid momentum equation resembling the 2-D forced Euler equation with a drag term.

$$nm_i \left(\frac{\partial}{\partial t} + \mathbf{v}_i \cdot \nabla \right) \mathbf{v}_i = -\nabla \tilde{p} - nm_i \nu_{in} \mathbf{v}_i + nm_i \mathbf{g} + nm_i \eta \nabla^2 \mathbf{v}_i \quad (3)$$

where $\tilde{p} = p_e + p_i + B\xi$ and where the electron drag term has been neglected.

We next solve (2) for the zeroth-order ion velocity, assuming an isothermal equation of state.

$$\mathbf{v}_i \approx \frac{1}{B} \hat{y} \times \nabla (\phi + T_i / e \ln n) + \frac{1}{\Omega_i} \mathbf{g} \times \hat{y} - \mu_i \nabla \phi - D_i \nabla \ln n \quad (4)$$

in which ϕ is the electrostatic potential, μ_i is the ion mobility $(\nu_{in} + d/dt)/\Omega_i B$, and D_i is the ion diffusivity $\nu_{in} T_i / e \Omega_i B$. Here, Ω_j refers to the gyrofrequency of species j. The two components of the mobility carry the ion Pedersen and polarization currents, respectively. The

geometry used is such that $\hat{x}$ is a unit vector in the eastward direction at the magnetic equator, $\hat{y}$ is in the direction of the geomagnetic field, and $\hat{z}$ is vertical. Let us further assume that $\mathbf{E} \times \mathbf{B}$ term with the small diamagnetic correction in (4) dominates the other terms and rewrite it in terms of a stream function ψ.

$$\mathbf{v}_i^0 = \hat{y} \times \nabla\psi \approx \mathbf{v}_i \tag{5}$$

$$\rho = \nabla \cdot (n\nabla\psi) = \hat{y} \cdot (\nabla \times n\mathbf{v}_i^0) \tag{6}$$

We have defined the generalized vorticity ρ, which is the component of the curl of the fluid momentum in the direction of the magnetic field. The dynamical equation for ρ can be derived by taking the $\hat{y}$ component of the curl of the single-fluid momentum equation [*Zargham*, 1988].

$$\left(\frac{\partial}{\partial t} + \mathbf{v}_i^0 \cdot \nabla\right)\rho + \frac{1}{2}(\hat{y} \times \nabla|\nabla\psi|^2) \cdot \nabla n = -\nu_{in}\rho + g\frac{\partial n}{\partial x} + \eta_* \nabla^2 \rho \tag{7}$$

In the *F* region ionosphere, the kinematic viscosity η is extremely small [*Kelley and Ott*, 1978]. The η_* term above is employed as a means of introducing the artificially inflated numerical viscosity required if simulations of the cutoff equations are to reproduce the turbulent behavior of continuous flows.

Finally, it can be shown by manipulating either the electron or ion continuity equation along with the quasineutrality condition and retaining electron collisional effects that the nearly incompressible plasma obeys a diffusion equation in which the ambipolar diffusion coefficient $D_a = (\mu_e D_i + \mu_i D_e)/(\mu_e + \mu_i)$ appears.

$$\frac{\partial n}{\partial t} + \mathbf{v}_i^0 \cdot \nabla n = D_a \nabla^2 n \tag{8}$$

In numerical computations, D_a will be replaced with a much larger numerical diffusion coefficient D_* for numerical stability.

If the ion-neutral collision frequency is sufficiently large that the entire left side of (7) is negligible by comparison, then the flow is in the collisional regime. In that case, (6), (7), and (8) specify the relatively simple dynamics of the collisional interchange instability that operates in the *F* region bottomside. This process produces highly coherent, anisotropic, quasi-sinusoidal, horizontally-propagating waves with vertically steepened boundaries. The resulting irregularities have been investigated in detail by several researchers (see for instance *Zalesak and Ossakow* [1980], *Keskinen et al.* [1980], *Zargham and Seyler* [1987], *Hysell et al.* [1994], and *Hysell and Kelley* [1997]).

Conversely, if the ion-neutral collision frequency is negligibly small and the left side of (7) must be retained, and if the amplitude of the density perturbations may be considered small, then (6) can be linearized, and the cubic terms on the left side of (7) can be neglected. In this case, the remainder of (7) becomes the vorticity form of the Navier Stokes equation in two dimensions. Since (8) is virtually decoupled from (7) in this limit, density irregularities become passive tracers of the turbulent flow. This is the basis for the argument that ordinary two-dimensional Navier Stokes turbulence might be operating in the topside ionosphere and that the velocity spectra of irregularities found there should obey the scaling laws predicted by *Kraichnan* [1967].

However, *McDaniel and Hysell* [1997] argued that this second limit never applies in the topside equatorial ionosphere. In order for plasma convection to be sufficiently strong for the left side of (7) to overcome the collisional term on the right side, the density irregularities that

ultimately force the convection must have substantial amplitudes. Linearization of (6) and the removal of cubicly nonlinear terms from (7) are consequently not justified in analyses or simulations of realistic inertial regime flows.

3. Numerical Model

We have performed numerical simulations of the model defined by (6), (7), and (8) using a hybrid code based on the one developed by *Zargham* [1988]. This code evaluates horizontal and vertical spatial derivatives using pseudospectral and finite difference methods, respectively. A semi-implicit leapfrog method is used for time advance. The code solves the linearized potential equation (6) with a tridiagonal solver and then uses Picard iteration to solve the full nonlinear equation. The runs we show here were conducted on a 256x256 grid. The boundary conditions imposed are periodic in the horizontal direction, Dirichlet on the lower boundary, and Neumann on the upper boundary.

Two simulations are shown here. For the first, the expression for the generalized vorticity in (6) was linearized, and the term to the left of the equal sign in (7) was discarded. These steps were also followed by *Zargham and Seyler* [1989] who derived the full model equations described in section 2 but neglected cubic nonlinearities in their simulation studies. What remains is a model for forced Navier Stokes turbulence. In simulating it, we recover the results of *Zargham and Seyler* [1989] for reference. Table 1 lists the dimensionless and dimensionalized parameters for the run. Note that anomalously high coefficients of molecular diffusion and viscosity are employed to maintain numerical stability. The dimensionalized simulation size is $2\pi \times 2$ km.

Table 1.

Figure 1.

Figure 1 shows the results from the simulation of the quadratically nonlinear model. The grayscale and surface plots are representations of the model plasma number densities at different simulation times. The initial condition on $n(\mathbf{x})$ for all our runs is depicted in the leftmost frame of the figure. The region where the background vertical density gradient is positive there can be interpreted as the leading edge of a deeply depleted region of plasma formed in the bottomside by the collisional interchange instability and convected into the topside. Broadband noise was introduced in a narrow horizontal strip where the linear growth rate of the interchange instability is greatest to initialize the simulation. By time step 40 (400 s), irregularities had grown from this noise to the point that a turbulent state had been achieved. At this time, simulation diagnostics showed that the total enstrophy (mean squared vorticity $\frac{1}{2}n_\circ \langle \rho^2 \rangle$) in the simulation had reached a steady-state value while the total kinetic energy per unit mass (mean squared velocity $\frac{1}{2}n_\circ \langle v^2 \rangle$) was still increasing approximately linearly. After about time step 50 (not shown), the positive vertical density gradient present at time step 0 was largely broken down by the instability, which consequently began to decay. The physical structures seen in the simulations are characteristic of two-dimensional Navier Stokes turbulence. They resemble circular caps trailing vortices from either side and are oriented approximately isotropically. The structures form through the rearrangement of the plasma density gradient present in the initial conditions, and their amplitudes are greater than 50% in this case.

One-dimensional energy density spectra corresponding to time steps 40 and 42 are shown in Figure 1 below the corresponding density plots. These are angle-averaged velocity spectra computed according to $P_1^E(k) = \frac{1}{2}\int k d\theta \, k^2 \psi^2(k,\theta)$, where θ is the polar angle in Fourier

space. The normalization of the spectra is arbitrary. These spectra clearly exhibit power-law behavior, indicating self-similarity in the flow. They show evidence of two inertial ranges at wavenumbers above and below approximately 20, respectively. Here, k=20 corresponds to a spatial scale size of approximately 628 m and signifies the injection wavenumber, the wavenumber where the instability growth rate is greatest. *Zargham and Seyler* [1989] estimated this wavenumber using a linear, nonlocal analysis. Their result was

$$k_m = \left(\frac{g}{4 L_n d^2 D_*^2} \right)^{1/6} \tag{9}$$

where L_n is the vertical gradient scale length and d is the vertical extent over which the background gradient exists. Given L_n = d = 0.25, (9) predicts k_m = 17.8 for this run.

The slopes of the two inertial ranges have been predicted by *Kraichnan* [1967] and *Kraichnan and Montgomery* [1980] on the basis of dimensional arguments and are indicative of energy and enstrophy cascade inertial ranges, respectively. A separation of scales is seen to exist, with energy and enstrophy being injected by the instability predominantly at the scale size of the spectral break. In the turbulent state, enstrophy is dissipated at the smallest scale sizes in the simulation by viscosity at the same rate it is injected, whereas energy accumulates at ever increasing scale sizes.

Table 2.

Table 2 lists the parameters used for the second simulation run. This time, (6) is not linearized, and all the terms in (7) are retained. By comparison to the values in Table 1, the forcing (g) has been halved for this run while the dissipation (D, η) has been doubled. The initial and boundary conditions remain the same.

Figure 2.

The results of the second simulation run are shown in Figure 2 for time steps when

a turbulent state has been reached. Corresponding, angle averaged, energy (mean-squared velocity) density spectra are shown for each time step. One difference from the preceding run is obvious: despite having reduced forcing and increased dissipation by comparison to the quadratic run, the cubic run developed more rapidly and reached a turbulent state in less time. This is a nonlinear effect predicted by (3). The time rate of change of the average kinetic energy in the simulation is given by

$$\langle n m_i \mathbf{g} \cdot \mathbf{v} \rangle \quad = \quad \langle n_\circ m_i \mathbf{g} \cdot \mathbf{v} \rangle + \langle \delta n \, m_i \mathbf{g} \cdot \mathbf{v} \rangle \tag{10}$$

where $n_\circ = \langle n \rangle$, $\delta n = n - n_\circ$, and where $\langle v \rangle = 0$. The third term in (10), which is proportional to $- \langle \delta n \, v_z \rangle$, is absent from the uniform density model but present in the complete model. Since irregularities in plasma density and velocity are almost perfectly anticorrelated in two-dimensional guiding center flows, the added term is apt to be quite important and can increase the growth rate of the instability well beyond its linear value. Morphologically, the structures that evolved in the simulation are similar to those in Figure 1. There is a subtle tendency for the structures that emerge in the cubicly nonlinear runs to be elongated by comparison to those in the quadratically nonlinear runs.

The one-dimensional spectra for the two simulation runs, meanwhile, are quite similar. Spectra computed from the cubic simulation obey power law scaling, indicating self similarity in the flow. Two power laws are again evident, with slopes close to -5/3 at large scales and -3 at small scales. These power laws were maintained between timestep 25, the time when the turbulence became fully developed, and timestep 30, the time when the background density gradient was exhausted and the flow began decaying. Such power laws are suggestive

of inertial ranges and turbulent cascades. The spectral break point once again occurs close to k=20. (The simulation parameters were chosen to make this so, permitting qualitative comparisons between the irregularity morphologies in the two runs.) Note that (9), which was based on a linear analysis, underestimates the spectral break point for this run.

Figure 3.

Figure 4.

The long-term behavior of the cubicly-nonlinear model simulation is depicted in Figure 3. In the early stages of the flow, nearly monochromatic waveforms appeared where the background density gradient was steepest. The wavelength of these waveforms corresponds to that of the fastest growing linear normal mode. As time progressed and the flow entered the nonlinear regime, these waveforms can be seen to have coalesced into a few large vortices. Such behavior is consistent with an inverse cascade of energy from intermediate to large spatial scales. At the same time, small-scale structure was generated by the stretching and convection of existing density irregularities into ever tightening vortices. This behavior is clearly illustrated by Figure 4, which compares in detail the plasma structures seen prior to and during the turbulent state. Note how monochromatic the initial structures appear to be, supporting the idea that forcing is supplied by a narrowband source. The turbulent flow depicted here became fully developed between time steps 25–30 but began to decay thereafter as the driving background density gradient was exhausted.

4. Analysis

Turbulent cascades arise in flows satisfying certain criteria (see for example *Tennekes and Lumley* [1972] and *Kintner and Seyler* [1985]). Among these are that the flow should be statistical in nature and not dominated by coherent structures. The flow should moreover

be statistically homogeneous and isotropic (translationally and rotationally invariant), at least locally. These kinematic requirements are prerequisite for ultimate self-similar scale invariance and the emergence of similarity spectra. Additional, dynamical requirements apply to the spectral characteristics of the flow. A separation of scales in Fourier space is required between the scales where mechanical stirring, provided by instability in this case, and dissipation take place. Apart from that, there must be a range or ranges of scale sizes where inertia is the dominant force on turbulent eddies which neither interact strongly with the mean flow nor suffer decorrelation due to viscosity. Insofar as a forward cascade is in question, this is tantamount to the requirement that the Reynolds number (ratio of fluid diffusivity to kinematic viscosity) be large ($\gtrsim 10^3$). The rate of injection of the cascaded quantity at the stirring scale must match the rate of cascade throughout the inertial range and the rate of dissipation at the dissipation scale, if applicable, for statistical equilibrium to occur. Finally, the nonlinear interactions bringing about the cascade are local in Fourier space, and the cascaded quantity must be conserved by those interactions. Turbulent cascades are characterized by coupling between adjacent modes in Fourier space. Coupling between widely separated modes is meanwhile associated with the convection of smaller eddies by larger ones but does not lead to decorrelation of the turbulent eddies involved.

If these conditions are met, then within the inertial ranges, the spectral density of the cascaded quantity will depend only on the rate of injection/cascade of that quantity and on the wavenumber. On dimensional grounds, the spectra of the velocity fluctuations in the flow within the inertial regimes then have predictable, power-law forms. In the case of two-dimensional turbulent flows with uniform densities, *Kraichnan* [1967] showed that

the kinetic energy (mean squared velocity) and enstrophy (mean squared vorticity) were "invariant" quantities, conserved by quadratically nonlinear interactions involving individual triads of wavevectors. These interactions give rise to two exclusive cascades: an inverse cascade of energy and a forward cascade of enstrophy. The associated power laws followed by the one-dimensional energy spectra were predicted to be -5/3 and -3, respectively. Numerous observations of turbulent flows in nature, and numerous numerical simulations, have borne out this prediction, including turbulent flows found in the ionosphere and magnetosphere (see *Kintner and Seyler* [1985]).

However, the nonlinear mode coupling in the flow in question here, which is nearly incompressible but nonuniform and which is modeled by equations with cubic nonlinearities, does not conserve either mean-squared velocity or mean-squared vorticity. In the appendix, it is shown that the kinetic energy per unit mass, $\frac{1}{2}\langle nv^2\rangle$, is invariant in the unforced, non-dissipative model limit. This cubicly nonlinear quantity can be expanded through Reynold's averaging as

$$\left\langle nv^2 \right\rangle \;=\; n_\circ \left\langle v^2 \right\rangle + \left\langle \delta n\, v^2 \right\rangle \tag{11}$$

Since velocity fluctuations in the magnetized plasma are highly correlated with density fluctuations (are, in fact, determined by them), we expect the triple correlation in (11) to be important and the energy to differ significantly from the quadratic mean squared velocity form. Furthermore, since the energy is a cubic quantity, there is no analogy to Parseval's theorem allowing its decomposition into simple, quadratic spectral components which can be summed in Fourier space to constitute the whole (see (A5)). Instead of by wave triplets,

energy is transported in Fourier space by nonlinear mode coupling involving wave quartets. The inability to decompose the energy invariant into localized spectral components would seem to violate the locality requirement and undermine cascade theory.

There are two conditions that would allow the assignment of a quantity of spectral energy to a specific wavevector. The first is that the spectrum of the plasma density be sharply peaked at $k = 0$. Since the sum of all the spectral components of $n(\mathbf{k})$ excluding the zero component cannot exceed the zero component if the density is to remain nonnegative in physical space, this condition can be met if the density fluctuations are broad banded. The other condition is that the correlation length of velocity fluctuations in Fourier space is extremely short so that different spectral components of the velocity field are uncorrelated. This condition should be satisfied if the flow field is stochastic and not dominated by coherent structures. Both conditions are consistent with the definition of turbulence.

Figure 5.

Figure 6.

In fact, both of these conditions are satisfied by the simulated flow depicted in Figure 2. Figure 5 shows the two-dimensional spectrum of the plasma density for simulation time step 27 when a turbulent state had been reached. The curve is very sharply peaked around k = 0 despite the fact that $\delta n/n$ approached unity in physical space at this time. Moreover, Figure 6 shows the autocorrelation function of the velocity fluctuations in Fourier space $\langle \mathbf{v}(\mathbf{k}') \cdot \mathbf{v}^*(\mathbf{k}' + \mathbf{k}) \rangle_{\mathbf{k}'}$. It too is sharply peaked at k = 0, indicating that the phasings of different spectral components of the flow velocity are uncorrelated except for interacting nearest neighbors. We have calculated the total kinetic energy for simulation time step 27 according to (A5) and found that half the energy is contained in contributions associated with the $n(0, 0)$ term. All but a very small amount of the remaining energy is contained in the

$n(0, \pm 1)$ terms. The most important new contribution to (11) evidently involves coupling between the velocity field and the background density gradient, even at an advanced stage of development of the interchange instability. Consequently, we can define the following quasi-local, real, symmetric expression for the spectral energy associated with wavevector $\mathbf{k}$:

$$\epsilon(\mathbf{k}) \approx \frac{1}{4} \sum_{\mathbf{k}'} \left[\mathbf{v}^*(\mathbf{k}) \cdot \mathbf{v}(\mathbf{k}+\mathbf{k}') + \mathbf{v}(\mathbf{k}) \cdot \mathbf{v}^*(\mathbf{k}+\mathbf{k}') \right] \chi(\mathbf{k}') \tag{12}$$

where $\mathbf{k}'$ is confined to a small set of wavevectors centered on the origin. Note that (12) has been written without a multiplicative factor of the ion mass and with the plasma density n contained within the low frequency plasma susceptibility $\chi = \omega_{pi}^2/\Omega_i^2$. Written this way, it has the same dimensions as the mean squared velocity. We assert that this quantity is sufficiently localized to undergo cascade and obey Kolmogorov scaling. One-dimensional, angle-averaged spectra computed from the simulation results according to (12) have the same shapes as those plotted in Figure 2.

We have sought another invariant for the nonuniform flow in the unforced, nondissipative limit related to the vorticity or to the generalized vorticity ρ, the curl of the momentum. In the appendix, we show that the generalized enstrophy, the mean squared generalized vorticity, is not strictly an invariant. (A8) in the appendix shows that this quantity is modified by a term which is fifth order nonlinear which arises from the convection of density irregularities. While generalized enstrophy is not conserved by the nonlinear mode coupling implied by (7) and (A6), it does, however, turn out to be nearly conserved by mode coupling.

Figure 7.

Figure 7 shows statistics gathered from the simulation of the complete model equations. The left panel shows the generalized energy and generalized enstrophy at different times in

the simulation. A turbulent state is achieved briefly during the period when the enstrophy is approximately constant, signifying a forward cascade with injection balancing dissipation, and the energy is still increasing, signifying an inverse cascade leading to accumulation at large scales. The right panel shows, as a function of simulation time, the ratio of the right side of (A8) to the total generalized enstrophy contained in the flow. This ratio is the growth time for the enstrophy due to the non-conservative term in the model equations. During the time that the turbulent state is achieved, the (non-dimensional) growth time falls between 10 and 20 time steps. By comparison, the eddy turnover time for eddies driven by the inertial interchange instability is $\tau \sim (kg)^{-1/2}$. This time is of order unity (non-dimensional) for the largest eddies in the simulation and decreases with increasing wavenumber. Since the growth time plotted in Figure 7 is always much larger than the eddy turnover time for even the largest eddies in the simulation, the generalized enstrophy can be regarded as an invariant quantity, conserved by nonlinear mode coupling for purposes of turbulence analysis.

Note that we have also simulated the flow described by (7) only neglecting the term immediately to the left of the equal sign. In this case, the generalized enstrophy is exactly conserved by mode coupling. The simulations revealed a flow that was essentially identical in its morphology and statistics (spectra) to the one depicted in Figure 2 and Figure 3. Evidently, the neglected term in question plays no important role in the fluid dynamics.

The generalized enstrophy is a quartic nonlinear quantity which is transported in Fourier space by means of the interactions of wave quintets. As is evident from (A9), it cannot be expressed uniquely as a simple sum of locally-defined spectral components. Making use of the facts that the density spectrum is sharply peaked around k = 0 and that the correlation length

of the stream function ψ in Fourier space is extremely short, we can truncate the sums in (A9) and define a quasi-local expression for the generalized enstrophy

$$\begin{aligned}\Omega(\mathbf{k}) \;\approx\; & \frac{1}{4}\sum_{\mathbf{k}'}\sum_{\mathbf{k}''}\mathbf{k}\cdot(\mathbf{k}+\mathbf{k}')(\mathbf{k}+\mathbf{k}'+\mathbf{k}'')\cdot(\mathbf{k}+\mathbf{k}') \\ & \left[\psi(\mathbf{k})\psi^*(\mathbf{k}+\mathbf{k}'+\mathbf{k}'')+\psi^*(\mathbf{k})\psi(\mathbf{k}+\mathbf{k}'+\mathbf{k}'')\right]\chi(\mathbf{k}')\chi(\mathbf{k}'')\end{aligned}$$

where only terms with $\mathbf{k}'$, $\mathbf{k}''$, and $|\mathbf{k}'+\mathbf{k}''|$ in a narrow band near the origin are included in the sums. This real, symmetric quantity is evidently sufficiently localized in Fourier space to undergo turbulent cascade. It is dimensionally identical to classical enstrophy, and the inertial range associated with its forward cascade consequently has the slope predicted by *Kraichnan* [1967].

5. Conclusion

Two-dimensional Navier Stokes turbulence occurs in the neutral atmosphere in flows with scale sizes exceeding the vertical scale height. It can occur in magnetized plasma flows where the scale size in one dimension is greatly elongated by the magnetic field. In the equatorial topside *F* region ionosphere, collisions dominate inertial forces in the momentum balance except when very dynamic flows are driven by strong density irregularities in ESF. We have generalized the equations of motion to allow for such irregularities. The resulting equations no longer conserve mean squared velocity and mean squared vorticity in the unforced, nondissipative limit. Nevertheless, numerical simulations of the initial value problem governed by the equations produce flows with velocity spectra exhibiting similarity ranges resembling those predicted for energy and enstrophy cascades in uniform

two-dimensional turbulent flows. The kinetic energy and generalized enstrophy are shown to be invariant or quasi-invariant under nonlinear interactions and dimensionally equivalent to the mean squared velocity and vorticity, respectively. Because of the statistical properties of the flow, these quantities are nearly localized in Fourier space despite being third and fourth order nonlinear. Thus, the turbulent cascade theories of *Kolmogorov* [1941], *Kraichnan* [1967], and *Batchelor* [1969] are sufficiently robust to apply to nonuniform plasma flows. The dimensional arguments which support the existence of inertial regimes with $k^{-5/3}$ and k^{-3} power law angle-averaged velocity spectra remain directly applicable.

Turbulent cascades arise from coupling between eddies in the flow with nearly the same scale size. The Fourier components of the velocity field, meanwhile, are plane waves and not eddies, and each eddy in the flow is associated with several Fourier components and the phase relationships between them. An eddy is a wave packet with a finite bandwidth in Fourier space. In guiding center plasma flows with strong density irregularities, the bandwidth of the eddies in Fourier space increases still further, but the cascade is not interrupted. We use Fourier decomposition for expediency, although other eigenfunctions are available [*Lumley*, 1970; *Moser*, 1994].

Equatorial spread *F* is important because of this dynamic range and intensity of observable effects on our environment, because of the spectacular and frequent nature of the large-scale plasma instabilities, and because of the variety of instruments that can be used to observe it. It has become more important lately because of its tendency to interfere with satellite-based communication and navigation systems. The plasma density irregularities we investigate here constitute a diffraction screen for radio waves passing between satellites and

the ground, and the resulting radio scintillations can cause severe communication distortion during spread *F* events, particularly when the irregularities penetrate to the topside. We need to study the spectrum of the irregularities in question to better understand the radio scintillations they can cause.

What are the implications for radio scintillations caused by ESF? Comparisons between the spectra of inertial and collisional regime irregularities in ESF are complicated by the facts that the latter are neither universal nor isotropic and that scintillation spectra and angle-averaged one-dimensional spectra are connected by a complex relationship and not directly comparable (see *Lovelace* [1970] and *Fredricks and Coroniti* [1976]). Radio amplitude scintillations are due mainly to ionospheric density irregularities at the Fresnel length which ranges between about 300 m and 1 km for UHF and L-band scintillations from topside irregularities. At such wavelengths, the spectra of density and transverse velocity fluctuations in ESF are proportional to each other and follow power laws with spectral indices close to -2 [*Hysell et al.*, 1994]. This slope is a consequence of the steepened, shock-like morphology of plasma structures in the collisional regime and the fact that a Heaviside function has a k^{-2} spectrum. This slope is somewhat steeper than that predicted for an energy cascade. Assuming that the intensity of the irregularities at the outer scale is the same, inertial regime flows will therefore tend to have more spectral content at the Fresnel length for scintillations than will collisional regime flows. Amplitude scintillations will consequently be stronger, interference more severe. Comparisons of satellite and scintillation receiver databases can be made to test this prediction.

Appendix A: Conservation properties

Here, we show that kinetic energy is conserved by the nonlinear interactions implied by the two-dimensional turbulence model presented in section 2 in the limit of purely incompressible, inviscid flow. When the driving and dissipative terms have been removed, the momentum equation (3) becomes:

$$nm_i \frac{\partial \mathbf{v}}{\partial t} + nm_i \left(\mathbf{v} \cdot \nabla\right) \mathbf{v} \;\; = \;\; -\nabla \tilde{p} \tag{A1}$$

where m_i is the ion mass, $\mathbf{v}$ is the guiding center plasma velocity, n is the plasma number density, and $\tilde{p}$ is the total pressure including the contribution associated with the $\mathbf{J} \times \mathbf{B}$ force. Taking the inner product of this equation with the velocity $\mathbf{v}$ gives:

$$nm_i \frac{\partial}{\partial t} \frac{v^2}{2} + nm_i \left(\mathbf{v} \cdot \nabla\right) \frac{v^2}{2} \;\; = \;\; -\nabla \tilde{p} \cdot \mathbf{v} \tag{A2}$$

which, when added to the continuity equation for the plasma (multiplied by a factor of $\frac{1}{2} m_i v^2$), yields an expression of the conservation of energy:

$$\frac{\partial}{\partial t} \epsilon + \nabla \cdot \left(\mathbf{v} \epsilon\right) \;\; = \;\; -\nabla \cdot \left(\tilde{p} \mathbf{v}\right) \tag{A3}$$

Note that the incompressibility of the guiding center velocity has been utilized in deriving (A3). In it, we identify $\epsilon(\mathbf{x}, t) = \frac{1}{2} m_i n v^2$ with the kinetic energy density in the plasma and $\mathbf{v}\epsilon$ with the energy flux. Local changes in the energy density arise either from the convection of energy from neighboring regions of space or from work done by pressure. Integrating (A3) over the entire volume containing the turbulent flow gives an expression for the time rate of change of the total kinetic energy in the medium:

$$\frac{d}{dt} \int_V d^2x \; \epsilon \;\; = \;\; -\oint_S ds \left(\epsilon + \tilde{p}\right) \mathbf{v} \cdot \hat{n} \tag{A4}$$

where the second integral is over the closed surface S surrounding the volume V. If the boundary conditions on S are either periodic, Dirichlet, or Neumann, the right side of (A4) vanishes, and the total energy in the volume is invariant. This condition is one for which pressure does no net work on the fluid. It is met, for example, if the volume is chosen to be sufficiently large such that the flow velocity vanishes on its boundary. Accordingly, the nonlinear interactions represented by the convective derivative in (A1) are shown to conserve energy, where the energy density has the cubic form $\frac{1}{2}m_i n v^2$.

In the Fourier domain, the total kinetic energy can be expressed as:

$$\int_V d^2x\, \epsilon \;\; = \;\; \frac{1}{2} m_i \sum_{\mathbf{k}_1} \sum_{\mathbf{k}_2} \mathbf{v}(\mathbf{k}_1) \cdot \mathbf{v}^*(\mathbf{k}_1 + \mathbf{k}_2) n(\mathbf{k}_2) \tag{A5}$$

where $\mathbf{k_1}$ and $\mathbf{k_2}$ are wavevectors and where it is assumed that the boundary conditions on S permit the deconstruction of the field quantities into harmonic basis functions. Note that the form of (A5) does not imply a quantity of spectral energy density associated with a single given wavevector component. That is, there is no uniquely defined quantity associates with a single wavevector which, when summed over all wavevectors, yields the energy in the system.

We turn next to properties of the generalized enstrophy, defined here as the mean squared generalized vorticity. The generalized vorticity equation, derived earlier in (7) and written here without its driving and dissipative terms, has the form:

$$\frac{\partial}{\partial t}\rho + \mathbf{v} \cdot \nabla \rho + \frac{1}{2}\left(\hat{y} \times \nabla |\nabla \psi|^2\right) \cdot \nabla n \;\; = \;\; 0 \tag{A6}$$

Multiplying this equation by ρ yields

$$\frac{\partial}{\partial t}\frac{\rho^2}{2} + \nabla \cdot \left(\mathbf{v}\frac{\rho^2}{2}\right) + \frac{1}{2}\hat{y} \cdot \left(\nabla |\nabla \psi|^2 \times \nabla n\right) \rho \;\; = \;\; 0 \tag{A7}$$

where incompressibility has again been invoked. Defining the generalized enstrophy by the quartic $\Omega(\mathbf{x},t)$=$\frac{1}{2}\rho^2$, we can write an expression for the time rate of change of the total enstrophy in the system as

$$\frac{d}{dt}\int_V d^2x\,\Omega \;=\; \frac{1}{2}\int_V d^2x \nabla\left[\hat{y}\cdot\left(\nabla|\nabla\psi|^2\times\nabla n\right)\right]\cdot\nabla\psi n \tag{A8}$$

where the divergence theorem has been applied to the second term in (A7), integration by parts has been applied to the third term, and where the boundary terms have vanished because of the choice of boundary conditions as above. However, the right side of (A8) is nonzero. Strictly speaking, the generalized enstrophy therefore does not appear to be an invariant for this systems and is not conserved by the cubicly-nonlinear mode coupling implied by (A6).

For the sake of completeness, we express the total generalized enstrophy in the Fourier domain below.

$$\int_V d^2x\,\Omega \tag{A9}$$
$$= \frac{1}{2}\sum_{\mathbf{k}_1}\sum_{\mathbf{k}_2}\sum_{\mathbf{k}_3}\mathbf{k}_3\cdot(\mathbf{k}_1+\mathbf{k}_3)(\mathbf{k}_1+\mathbf{k}_2+\mathbf{k}_3)\cdot(\mathbf{k}_1+\mathbf{k}_3)n(\mathbf{k}_1)n(\mathbf{k}_2)\psi(\mathbf{k}_3)\psi^*(\mathbf{k}_1+\mathbf{k}_2+\mathbf{k}_3)$$

One again, we note that there is no uniquely defined quantity associated with a single wavevector which, when summed over all wavevectors, yields the total enstrophy in the system.

Acknowledgments. This work was supported by the National Aeronautics and Space Administration through grant NAG5-9267 to Clemson University.

References

Batchelor, G. K., Computation of the energy spectrum in homogenous two-dimensional turbulence: High speed computing in fluid dynamics, *Phys. Fluids, Suppl. II*, p. 233, 1969.

Fredricks, R. W., and F. V. Coroniti, Ambiguities in the deduction of rest frame fluctuation spectrums from spectrums computed in moving frames, *J. Geophys. Res.*, *81*, 5591, 1976.

Haerendel, G., Theory of equatorial spread *F*, Max-Planck Institute für Physik und Astrophysik, Garching, West Germany, 1973, preprint.

Hassam, A. B., W. Hall, J. D. Huba, and M. J. Keskinen, Spectral characteristics of interchange instability, *J. Geophys. Res.*, *91*, 13,513, 1986.

Hossain, M., W. H. Matthaeus, and D. Montgomery, Long-time states of inverse cascades in the presence of a maximum length scale, *J. Plasma Phys.*, *30*, 479, 1983.

Hysell, D. L., and M. C. Kelley, Decaying equatorial *F* region plasma depletions, *J. Geophys. Res.*, *102*, 20,007, 1997.

Hysell, D. L., C. E. Seyler, and M. C. Kelley, Steepened structures in equatorial spread *F*, 2, Theory, *J. Geophys. Res.*, *99*, 8841, 1994.

Jahn, J. M., and J. LaBelle, Dc electric field measurements with the Guará spread-F rocket, *Geophys. Res. Lett.*, *24*, 1695, 1997.

Jahn, J. M., and J. LaBelle, Rocket measurements of high-altitude spread *F* irregularities at the magnetic dip equator, *J. Geophys. Res.*, *103*, 23,427, 1998.

Kelley, M. C., and E. Ott, Two-dimensional turbulence in the equatorial spread *F*., *J. Geophys. Res.*, *83*, 4369, 1978.

Keskinen, M. J., S. L. Ossakow, and P. K. Chaturvedi, Preliminary report of numerical simulations of intermediate wavelength collisional Rayleigh-Taylor instability in equatorial spread *F*, *J. Geophys. Res.*, *85*, 1775, 1980.

Kintner, P. M., and C. E. Seyler, The status of observations and theory of high-latitude ionospheric and magnetospheric plasma turbulence, *Space Sci. Rev.*, *41*, 91, 1985.

Kolmogorov, A. N., The local structure of turbulence in incompressible viscous fluids for very high Reynolds numbers, *Compti. Ren. Acad. Sci. U.S.S.R.*, *30*, 301, 1941.

Kraichnan, R. H., Inertial ranges in two-dimensional turbulence, *Phys. Fluids*, *10*, 1417, 1967.

Kraichnan, R. H., and D. Montgomery, Two-dimensional turbulence, *Rep. Prog. Phys.*, *43*, 547, 1980.

Lovelace, R. V. E., Theory and analysis of interplanetary scintillations, Ph.D. thesis, Cornell Univ., 1970.

Lumley, J. L., *Stochastic Tools in Turbulence*, Academic Press, New York, 1970.

Matthaeus, W. H., W. T. Stribling, D. Martinez, S. Oughton, and D. Montgomery, Selective decay and coherent vortices in two-dimensional incompressible turbulence, *Phys. Rev. Lett.*, *66*, 2731, 1991.

McDaniel, R. D., and D. L. Hysell, Models and DE II observations of inertial-regime irregularities in equatorial spread *F*, *J. Geophys. Res.*, *102*, 22,233, 1997.

Montgomery, D., W. H. Matthaeus, W. T. Stribling, D. Martinez, and S. Oughton, Relaxation in two dimensions and the “sinh-Poisson” equation, *Phys. Fluids A*, *4*, 3, 1992.

Moser, R. D., Kolmogorov inertial range spectra for inhomogenous turbulence, *Phys. Fluids*, *6*, 794, 1994.

Ossakow, S. L., Spread *F* theories – A review, *J. Atmos. Terr. Phys.*, *43*, 437, 1981.

Ott, E., Theory of Rayleigh-Taylor bubbles in the equatorial ionosphere, *J. Geophys. Res.*, *83*, 2066, 1978.

Stanisic, M. M., *The Mathematical Theory of Turbulence,* Springer Verlag, New York, 1988.

Sultan, P. J., Linear theory and modeling of the Rayleigh-Taylor instability leading to the occurrence of equatorial spread *F*, *J. Geophys. Res.*, *101*, 26,875, 1996.

Tennekes, H., and J. L. Lumley, *A First Course in Turbulence,* The M.I.T. Press, Cambridge, Mass., 1972.

Van Beeck, J. P. A. J., and C. Benocci (Eds.), *Introduction to the Modelling of Turbulence,* Lecture series 2000-04, von Karman Institute, Rhode Saint Gen‘ese, Belgium, 2000.

Woodman, R. F., and C. La Hoz, Radar observations of *F* region equatorial irregularities, *J. Geophys. Res.*, *81*, 5447, 1976.

Zalesak, S. T., and S. L. Ossakow, Nonlinear equatorial spread *F*: Spatially large bubbles resulting from large horizontal scale initial perturbations, *J. Geophys. Res.*, *85*, 2131, 1980.

Zargham, S., Numerical simulations of the ionospheric interchange instability, Ph.D. thesis, Cornell Univ., Ithaca, N. Y., 1988.

Zargham, S., and C. E. Seyler, Collisional interchange instability, 1, Numerical simulations of intermediate-scale irregularities, *J. Geophys. Res.*, *92*, 10,073, 1987.

Zargham, S., and C. E. Seyler, Collisional and inertial dynamics of the ionospheric interchange instability, *J. Geophys. Res.*, *94*, 9009, 1989.

Zhou, Y., and W. H. Matthaeus, Models of inertial range spectra of interplanetary magnetohydrodynamic turbulence, *J. Geophys. Res.*, *95*, 14,881, 1990.

---

205 Kinard Lab, Department of Physics and Astronomy, Clemson University, Clemson, SC 29634. e-mail: dhysell@clemson.edu

Received X; revised X; accepted X.

To appear in JGR, 2001

This manuscript was prepared with AGU's LaTeX macros v5, with the extension package 'AGU++' by P. W. Daly, version 1.6b from 1999/08/19.

Figure Captions

Figure 1. Simulation of quadratically nonlinear model equations. Grayscale and surface plots both represent relative plasma number density. Below them are plotted one-dimensional energy density spectra (see text). Dashed lines with slopes of -5/3 and -5 have been superimposed on the spectra to help guide the eye.

Figure 2. Simulation of cubicly nonlinear model equations.

Figure 3. Long-term behavior of the cubicly nonlinear model simulation.

Figure 4. Expanded view of the turbulent structures at two simulation timesteps. An area one quarter the size of the total simulation space is shown in each case.

Figure 5. Fourier-space spectrum of plasma density for simulation time step 27. The origin of the plot is at its center. Both axes span values from -128 to +127. The normalization of the plot is arbitrary.

Figure 6. Fourier-space autocorrelation function of plasma velocity for simulation time step 27. The origin of the plot is at its center. Both axes span values from -128 to +127. The normalization of the plot is arbitrary.

Figure 7. (Left) Average generalized energy (solid line) and generalized enstrophy (dashed line) for the cubic simulation. (Right) Time scale for enstrophy variations in nondimensional time units (see text).

Tables

Table 1. Quadratic Simulation Parameters.

256x256 Grid	Nondimensional	Dimensional
Length scale	1 l	2 km
Time scale	1 t	10 s
Simulation size	2π l	$2\pi \cdot$ 2 km
g	0.5 l/t^2	10 m/s^2
ν_{in}	0.1 t^{-1}	0.01 s^{-1}
D_*	5.0x10^{-4} l^2/t	200 m^2/s
η_*	2.5x10^{-5} l^2/t	10 m^2/s
Time step	2.5x10^{-3} t	0.025 s
Grid spacing	2π/256 l	49 m

Table 2. Cubic Simulation Parameters.

256x256 Grid	Nondimensional	Dimensional
Length scale	1 l	2 km
Time scale	1 t	10 s
Simulation size	2π l	$2\pi \cdot$ 2 km
g	0.25 l/t^2	5 m/s^2
ν_{in}	0.1 t^{-1}	0.01 s^{-1}
D_*	1.0x10^{-3} l^2/t	400 m^2/s
η_*	5.0x10^{-5} l^2/t	20 m^2/s
Time step	2.5x10^{-3} t	0.025 s
Grid spacing	2π/256 l	49 m

Figures

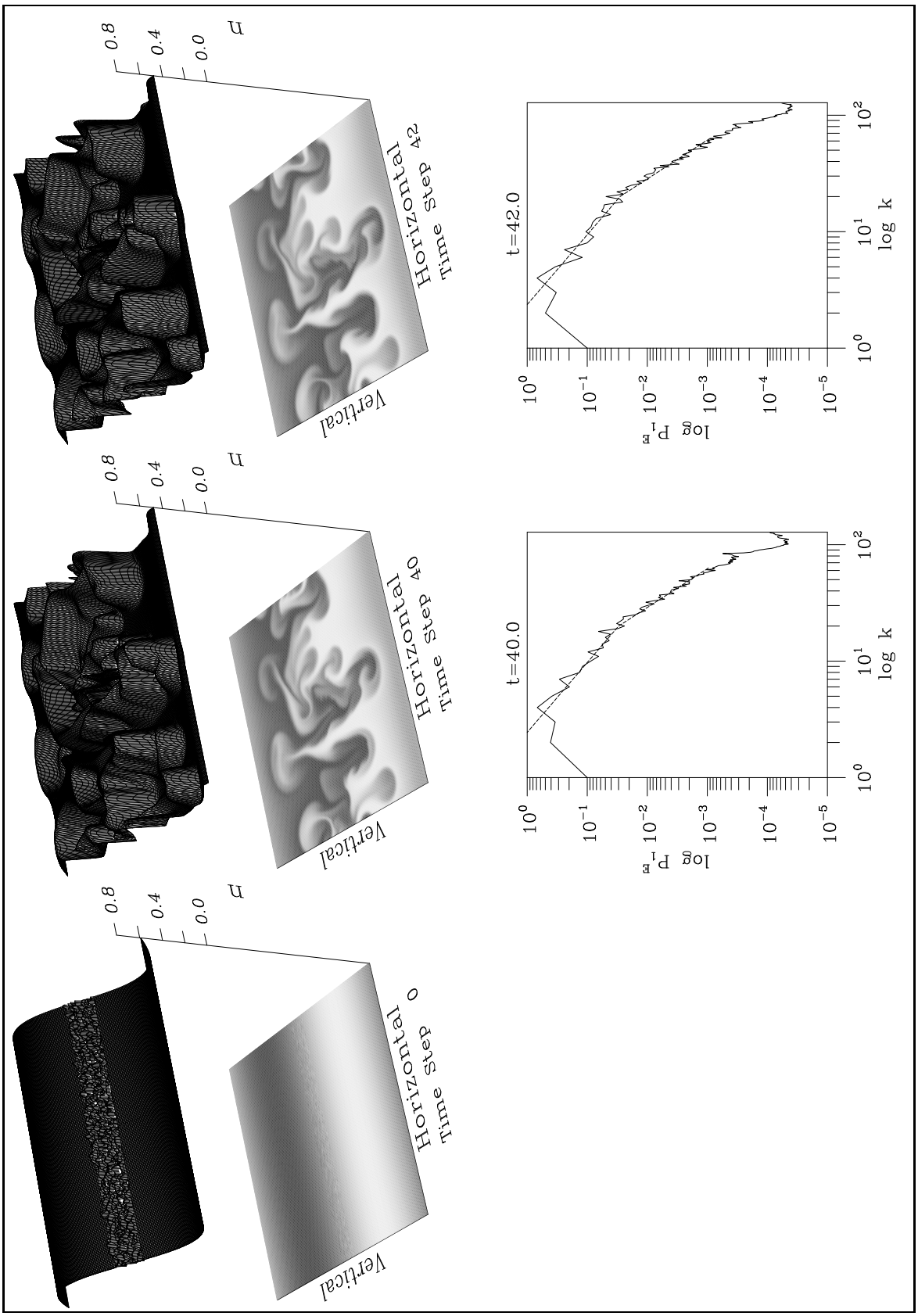

Figure 1. Simulation of quadratically nonlinear model equations. Grayscale and surface plots both represent relative plasma number density. Below them are plotted one-dimensional energy

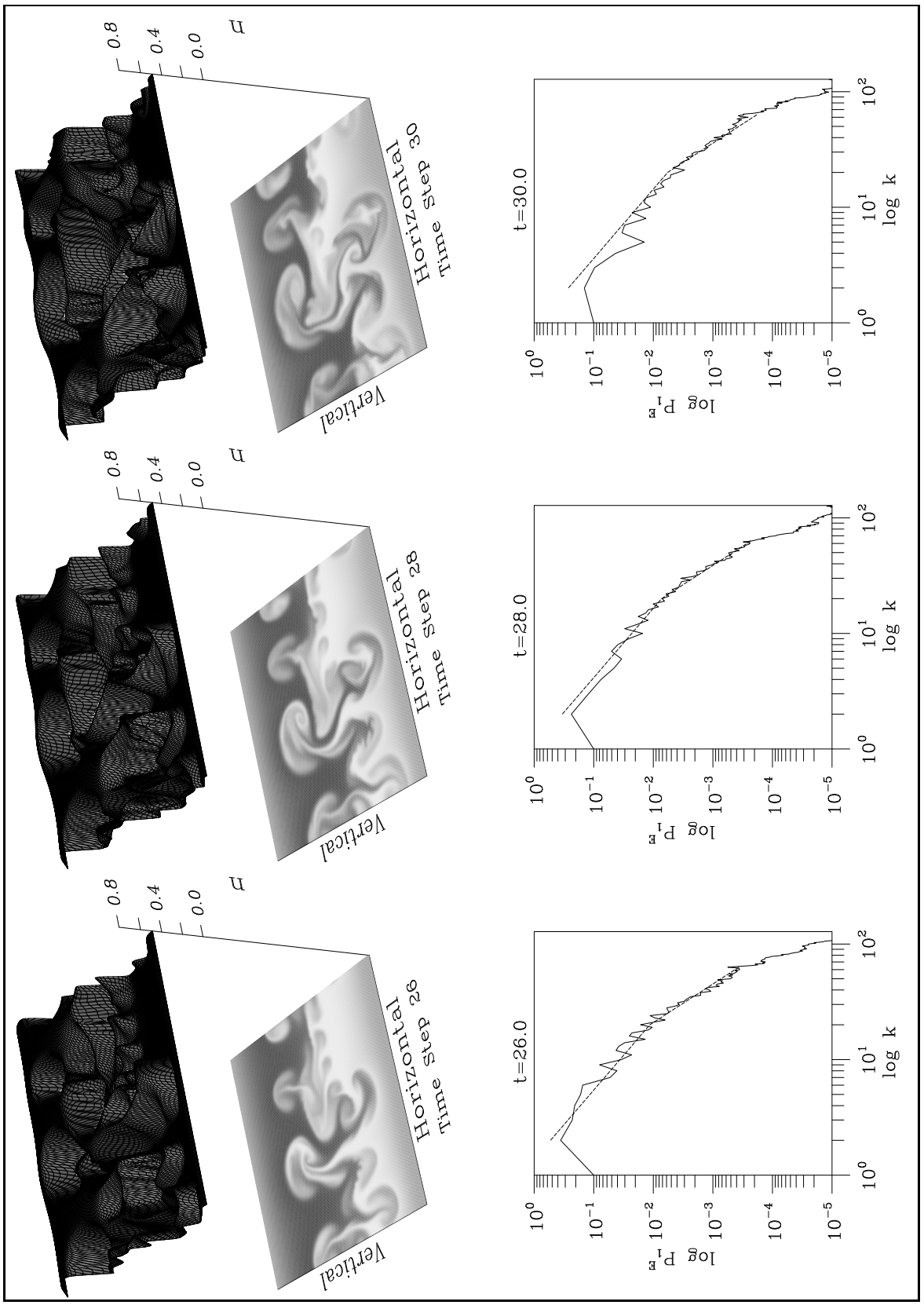

Figure 2. Simulation of cubicly nonlinear model equations.

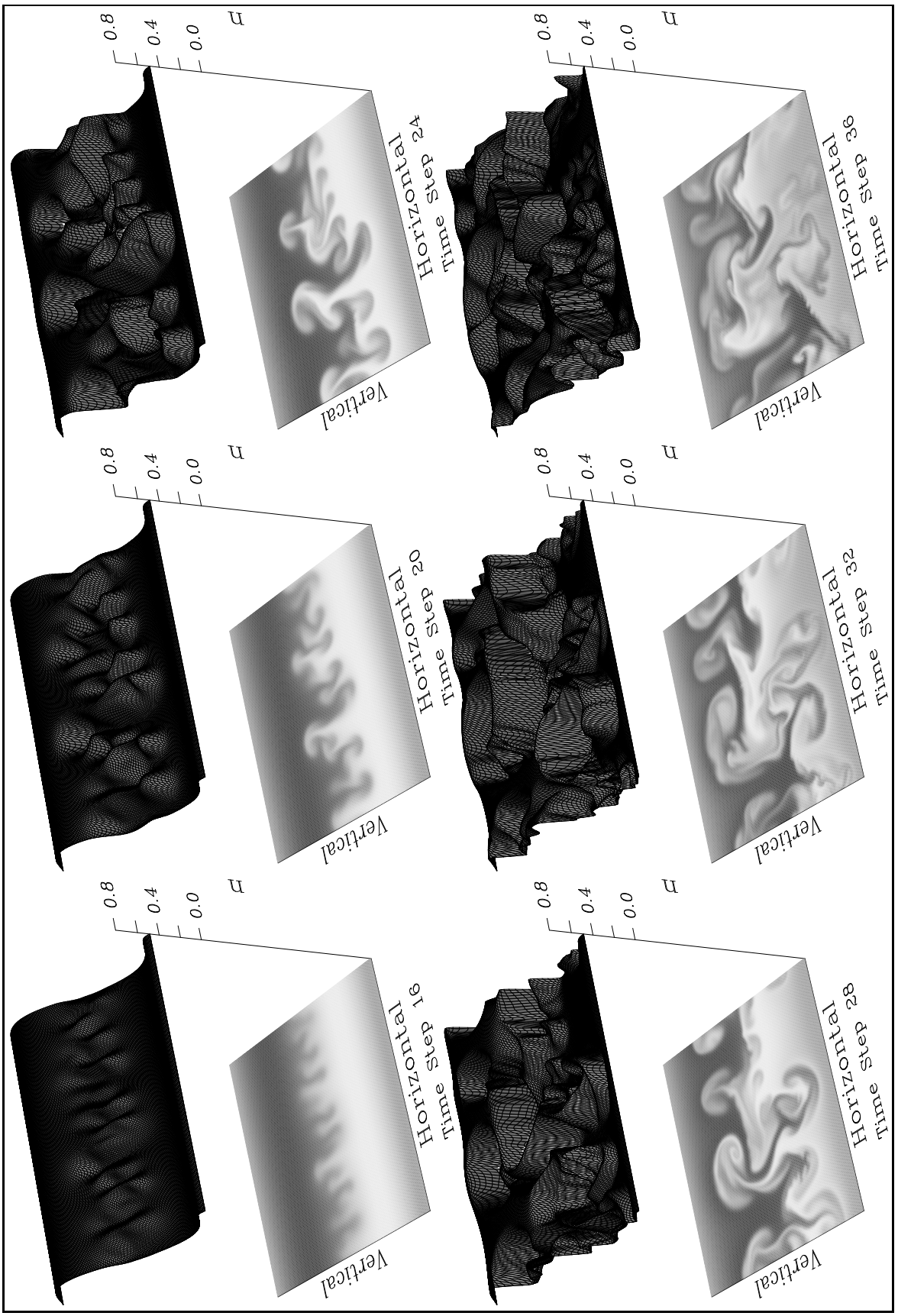

Figure 3. Long-term behavior of the cubicly nonlinear model simulation.

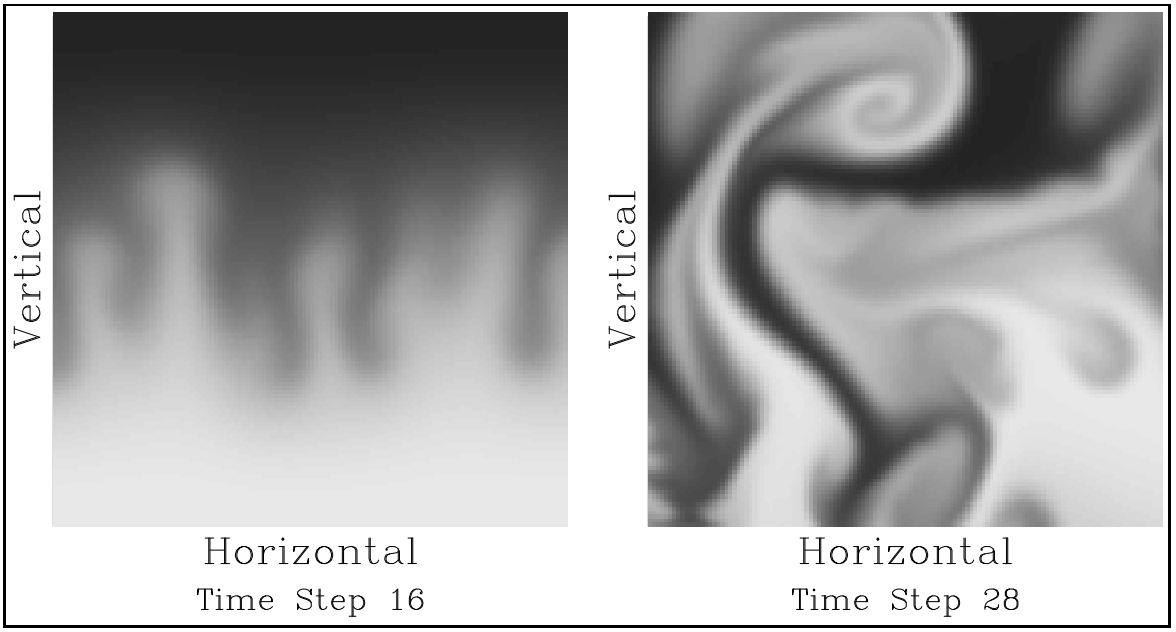

Figure 4. Expanded view of the turbulent structures at two simulation timesteps. An area one quarter the size of the total simulation space is shown in each case.

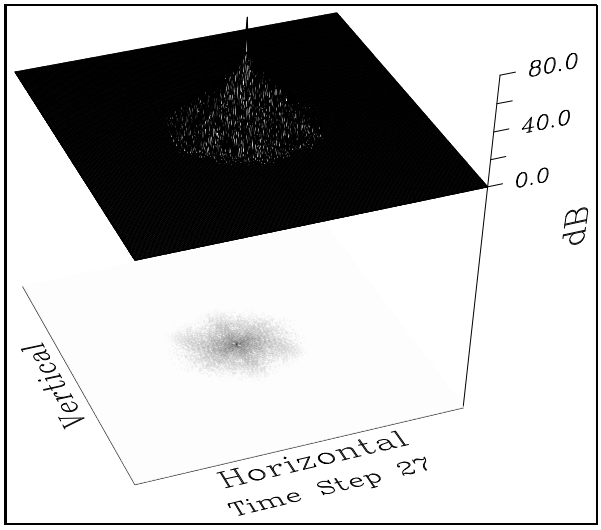

Figure 5. Fourier-space spectrum of plasma density for simulation time step 27. The origin of the plot is at its center. Both axes span values from -128 to +127. The normalization of the plot is arbitrary.

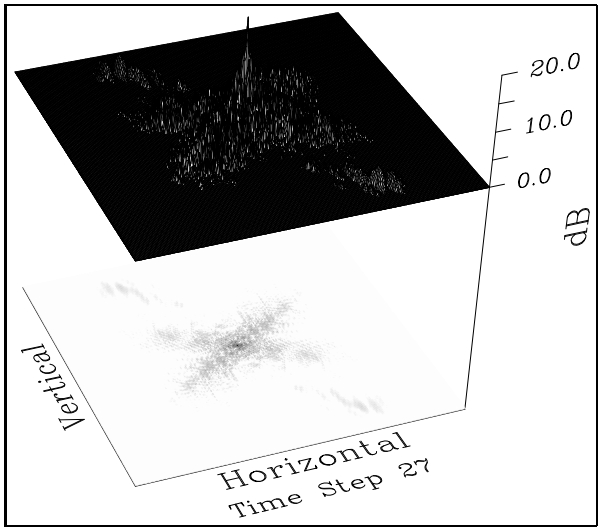

Figure 6. Fourier-space autocorrelation function of plasma velocity for simulation time step 27. The origin of the plot is at its center. Both axes span values from -128 to +127. The normalization of the plot is arbitrary.

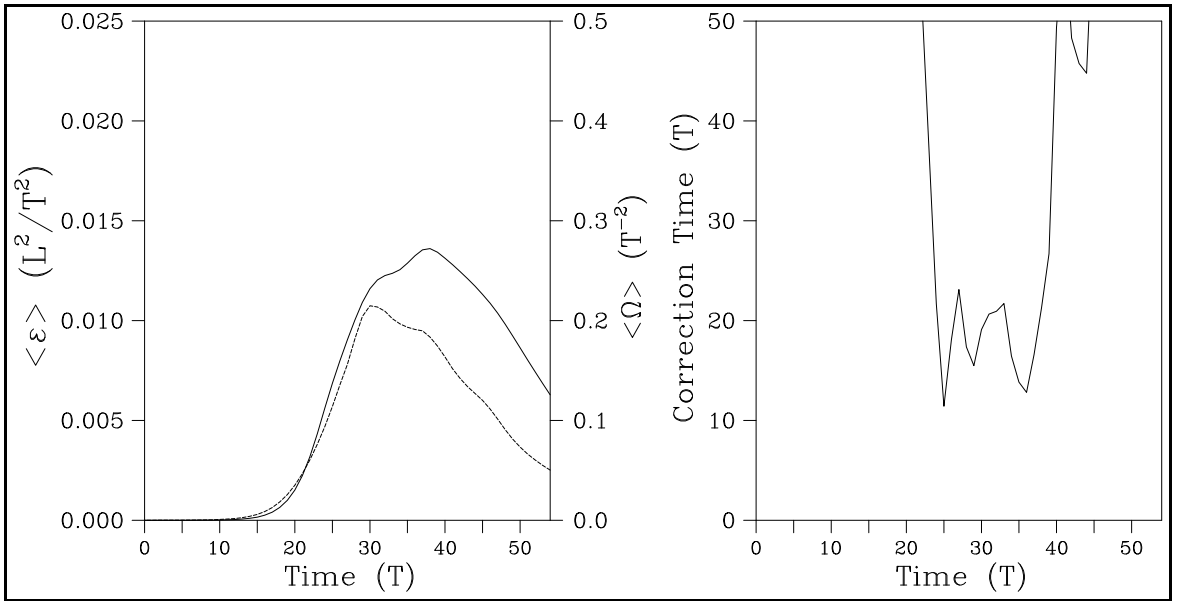

Figure 7. (Left) Average generalized energy (solid line) and generalized enstrophy (dashed line) for the cubic simulation. (Right) Time scale for enstrophy variations in nondimensional time units (see text).